Feedbacks between subduction dynamics and slab deformation: Combined effects of nonlinear rheology of a weak decoupling layer and phase transitions

Jakub Pokorný [a],[*], Hana Čížková [a], Arie van den Berg [b]

[a] *Charles University Prague, Faculty of Mathematics and Physics, Department of Geophysics, Czech Republic*
[b] *Utrecht University, Institute of Earth Sciences, Department of Theoretical Geophysics, Netherlands*

ABSTRACT

Seismic tomography reveals a wide variety of slab deformation in the mantle transition zone and shallow lower mantle. Numerical modeling of subduction has identified several factors that control slab deformation, among them the properties of the mechanical decoupling between subducting and overriding plates was shown to have a major influence on slab velocity, rollback and deformation in the transition zone. Models with weak crust generally yield fast rollback and slab stagnation while stronger crust results in slab penetration into the lower mantle. Here we perform a detailed analysis of the effects of this weak crustal layer. First, in models with constant crustal viscosity, we quantify combined effects of crustal viscosity and thickness. Further we apply nonlinear crustal rheology that combines dislocation creep and pseudoplastic deformation. We test the effects of varying parameterisations of the nonlinear rheological mechanisms and evaluate their effects on slab deformation. We conclude that the variations of subducting slab velocity (controlled by the buoyancy effects of the major phase transitions) induce strong time variations of the crustal viscosity that in turn enforce further acceleration or deceleration of the slab. This feedback between slab velocity and crustal viscosity strenghtens transient behavior of the subducting slabs and enforces slab penetration after a transient period of stagnation.

1. Introduction

The main source of information about the deformation of subducting slabs in the Earth mantle is seismic tomography (Bijwaard et al., 1998; Fukao and Obayashi, 2013; Zhao et al., 2017; van der Meer et al., 2018). It shows that though some subducting slabs directly penetrate the lower mantle, in most subduction areas they are significantly deformed in the lower part of the upper mantle and at least temporarily delayed in this region (Goes et al., 2017). Subduction of lithospheric plates is a highly complex geodynamical problem affected by many factors and the effects that control slab stagnation/penetration have been studied in numerous modeling studies. The primary control is exerted by slab and mantle rheology (e.g. Čížková et al., 2002; Billen and Hirth, 2007) and effects of phase transitions (e.g. Christensen, 1996; Schmeling et al., 1999; van Hunen et al., 2001; Bina et al., 2001; Torii and Yoshioka, 2007; Billen, 2010; Arredondo and Billen, 2017; Holt et al., 2015; Faccenda and Zilio, 2017; Goes et al., 2017). As the slab stagnation/penetration is closely related to trench migration (Čížková and Bina, 2019), also the processes

occuring at shallow depths such as e.g. dehydratation of the subducting material that affects both viscosity and density in proximity of the slab at shallow depths (Arcay et al., 2005; Iwamori, 2007; Duarte et al., 2015; Nakao et al., 2016, 2018), slab stiffness and its viscosity contrast with respect to the mantle (e.g. Ribe, 2010; Stegman et al., 2010) or the properties of the overriding plate (Garel et al., 2014; Holt et al., 2015) were shown to play important role.

Among other parameters, the properties of the mechanical decoupling between subducting and overriding plate have been shown to have major influence on the subducting slab behavior. A thin weak layer, often refered to as the crust, lowers the friction at the contact and facilitates subduction (Běhounková and Čížková, 2008; Chertova et al., 2012; Agrusta et al., 2014). The decoupling effect of such a weak zone may be affected by the abundance of sediments on the top of the subducting plate. Presence of the sedimentary layer may reduce the weak zone viscosity by 1–2 orders of magnitude relative to the astenosphere. This softening allows faster plate velocities and can thus affect the whole subducting dynamics (Behr and Becker, 2018). Models with constant

---

crustal viscosity have already shown, that magnitude of the crustal viscosity plays an important role in determining the subducting plate velocity (Androvičová et al., 2013) and also in terms of its deformation in the transition zone and the ability of the slab to penetrate the lower mantle (Čížková and Bina, 2013; Goes et al., 2017). Furthermore low-viscosity crust allows effective decoupling of the plates and results in faster rollback. Enhancement of rollback is associated with stagnation of the slab above the endothermic phase transition at 660 km depth (Torii and Yoshioka, 2007; Agrusta et al., 2017; Čížková and Bina, 2019). On the other hand high-viscosity of the crust suppresses rollback and thereby facilitates slab penetration into the lower mantle.

Here we will further elaborate on the effects of the rheological properties of the (crustal) decoupling layer to the slab deformation. First, we will discuss in more detail the models with constant crustal viscosity and demonstrate the effects of its thickness. We will quantify the combined effect of these two parameters on the slab behavior by introducing a resistance parameter that controls the lubricating effect of a weak crustal layer, and evaluate slab stagnation/penetration in connection with this crustal resistance.

Using constant crustal viscosity may be a numerical convenience that allows plate decoupling without reflecting the real constitution law of crustal materials. It has however been shown in crustal rock experiments that crust deforms nonlinearly under the temperature and pressure conditions of subduction (Ranalli, 1995; Shelton and Tullis, 1981). Therefore in the second part of the paper we will assume that the crustal layer deforms nonlinearly through dislocation creep and stress-limiting Byerlee type pseudoplastic deformation. We will then demonstrate how the feedback between slab velocity and a nonlinear strainrate dependent crustal viscosity affects slab penetration/stagnation at 660 km depth. Finally, we will adress the effect of phase transitions in the models with nonlinear crustal rheology.

2. Model setup

We solve the system of partial differential equations describing convection in the Earth's mantle in an extended Boussinesq approximation (EBA, Ita and King, 1994) without internal heating. Numerical solution of the governing equations is obtained with the SEPRAN finite element toolkit (Segal and Praagman, 2005; van den Berg et al., 2015).

Our 2D Cartesian model domain is 10,000 km wide and covers a region from the surface to 2000 km depth. The subducting lithospheric plate stretches from a mid-ocean ridge situated in the upper left corner to the trench located in the middle of the model domain. The age of the subducting plate follows a halfspace model and reaches the age of 100 Ma at the trench. The overriding plate stretches from the second mid-ocean ridge in the upper right corner and has the same age as the subducting plate. An initial temperature distribution (Fig. 1a) is obtained in a short (6 Ma) preliminary run where a constant convergence velocity of 2.5 cm/year is prescribed on the top of the subducting plate. During this pre-run the tip of the subducting plate is driven to a depth of 200 km (Fig. 1a). Then the kinematic boundary condition is switched off and an impermeable free slip is prescribed on all boundaries. Thermal boundary conditions include reflective side boundaries and constant temperature prescribed at the top (273 K) and at the bottom of the model domain (2132 K). Density anomalies in our EBA model are linearly proportional to temperature anomalies with reference density $\rho_0 = 3416$ kg/m^3 and depth dependent thermal expansivity (Katsura et al., 2009). Thermal expansivity varies with depth from 3×10^{-5} K^{-1} at the surface to 1.2×10^{-5} K^{-1} at the depth of 2000 km at the bottom of the model domain (Hansen et al., 1993). Thermal diffusivity is held constant 10^{-6} m^2 s^{-1}. An increase of initial temperature with depth is illustrated in Fig. 1b.

Mechanical decoupling of the two plates is facilitated by a low-viscosity layer prescribed on the top of the subducting plate. Such a weak layer is often used in subduction modeling as a numerical
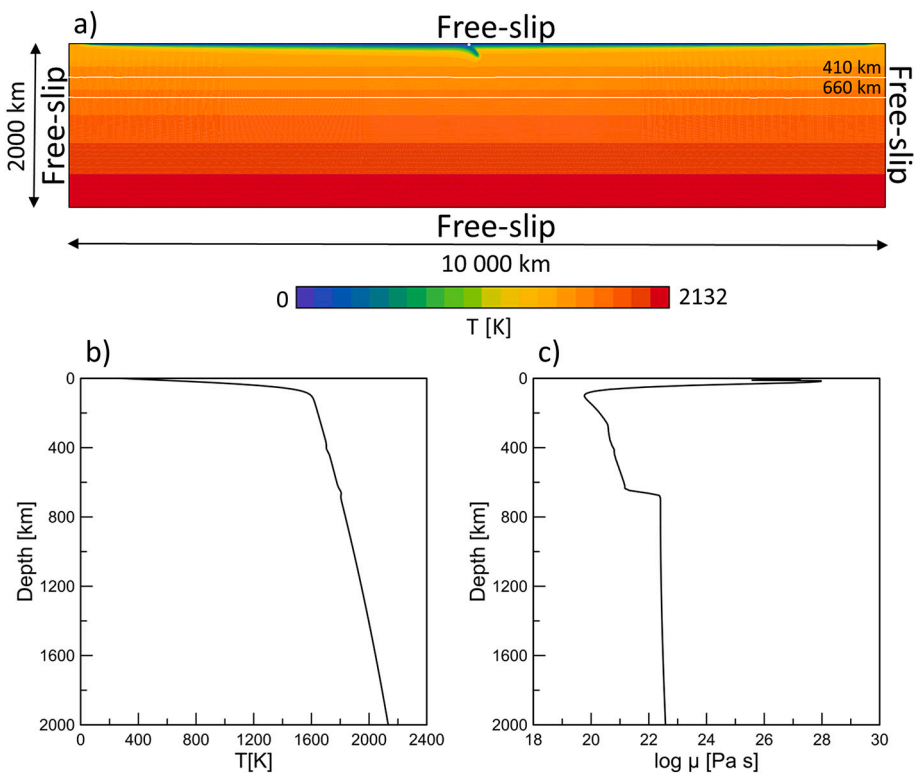
Fig. 1. Panel a): Model setup and initial temperature. Model domain is 2000 km deep and 10,000 km wide. At all boundaries an impermeable free slip is prescribed. White lines indicate the position of the major mantle phase transitions. Panel b): Vertical profile of temperature at x = 2000 km from the ridge. Panel c): Vertical profile of viscosity at x = 2000 km from the ridge.

convenience that allows relative sliding of the two plates. It should mimick the effects of a weak crust that has rather complex structure with a fine sediment layer at the top and presumably upper and lower crustal layers with different rheological properties underlying it (Liao et al., 2017). In the present paper we approximate this complex decoupling structure by a single layer of weak material with uniform properties. The crustal material is advected using 10^6 material tracers initially positioned within the crust and its near neighbourhood. Crustal tracers are laid along the surface of the subducting plate from the mid-ocean ridge in the upper-left corner to the trench at the contact of subducting and overriding plates 5000 km from the ridge. Crustal tracers are not being added during the model evolution which means that when this 5000 km long subducting plate was subducted and all weak crust was consumed, the subducting plate would get locked and subduction would terminate. All our model runs are stopped before that moment. At the depth of 150 km where the decoupling effect of a weak layer is no more needed, the viscosity of the decoupling layer is replaced by mantle viscosity for numerical convenience. Spatial resolution of the finite element mesh varies within the model domain. Maximum resolution of 3 km is in the contact area of the plates up to the depth of 200 km, the resolution in the transition zone and upper part of the lower mantle is 10 km and then the element size is growing towards the boundaries of the model domain.

The main mantle phase transitions, i.e. exothermic at 410 km depth, where the polymorphous transition from forsterite to wadsleyite takes place, and endothermic at 660 km depth, where ringwoodite changes to bridgmanite and periclase, are included in the model. We take into account both the buoyancy and latent heat effects associated with these transitions. Since the limitation of mantle material to olivine may overestimate the effects of the phase transition (Arredondo and Billen, 2016) and taking into account the uncertainties in the evaluation of the Clapeyron slopes, we test its effects by varying both γ_{410} (1 MPa/K, 2 MPa/K) and γ_{660} (−1.5 MPa/K, −2.5 MPa/K). Density contrast associated with the 410 km and 660 km phase transitions is 8 and 10% respectively (see Table 1). Phase transitions are implemented using a phase function (Christensen and Yuen, 1985) with harmonic parameterization (Čížková et al., 2007).

In order to evaluate some characteristic model quantities in the postprocessing phase we make use of passive (monitor) material tracers. A first group of these monitor tracers is prescribed in the crust and is used to calculate the average viscosity of this decoupling layer. Initially 8000 tracers are evenly distributed within the crust. In order to calculate the average viscosity at the contact of the plates, we divide all crustal tracers that are at certain moment in the depth interval of 15–100 km into 15 km depth subintervals and calculate the harmonic average of viscosity in these subintervals. Geometric mean of these values is then used to produce one characteristic crustal viscosity. The second group of passive tracers is placed within the subcrustal subducting lithospheric plate. These tracers are then used to determine the penetration depth of the slab. In every timestep we simply identify the deepest tracer from this second group. Finally, a single tracer initially positioned in the overriding plate to the right from the trench is used to monitor trench velocity.

3. Rheology

In our models we assume two materials, mantle (including the lithospheric plates) and crust. The rheology of the mantle material is described by a composite model (van den Berg et al., 1993; Čížková et al., 2002), where the effective viscosity combines three deformation mechanisms: diffusion creep, dislocation creep and a power-law stress limiter as an approximation of Peierls creep (Androvičová et al., 2013). The viscosities of the individual creep mechanisms are defined as follows. Diffusion creep viscosity is

$$\eta_{diff} = A_{diff}^{-1} exp\left(\frac{E_{diff} + pV_{diff}}{RT}\right) \quad , \tag{1}$$

Table 1
Model parameters.

Symbol	Meaning	Value	Units
Upper mantle and oceanic lithosphere rheology			
A_{diff}	Pre-exponential parameter of diffusion creep[a]	1×10^{-9}	$Pa^{-1}\ s^{-1}$
A_{disl}	Pre-exponential parameter of dislocation creep[a]	31.5×10^{-18}	$Pa^{-n}\ s^{-1}$
E_{diff}	Activation energy of diffusion creep[a]	3.35×10^5	$J\ mol^{-1}$
E_{disl}	Activation energy of dislocation creep[a]	4.8×10^5	$J\ mol^{-1}$
V_{diff}	Activation volume of diffusion creep[a]	4.0×10^{-6}	$m^3\ mol^{-1}$
V_{disl}	Activation volume of dislocation creep[a]	11×10^{-6}	$m^3\ mol^{-1}$
η_{diff}	Viscosity of diffusion creep	–	$Pa\ s$
η_{disl}	Viscosity of dislocation creep	–	$Pa\ s$
η_y	Power-law stress limitor viscosity	–	$Pa\ s$
n	dislocation creep exponent	3.5	–
$\dot{\varepsilon}_y$	Reference strain rate	1×10^{-15}	s^{-1}
σ_y	Stress limit	$2 - 5 \times 10^8$	Pa
p	Hydrostatic pressure	–	Pa
n_y	Stress limit exponent	10	–
R	Gas constant	8.314	$J\ K^{-1}\ mol^{-1}$
T	Temperature	–	K
$\dot{\varepsilon}_\parallel$	Second invariant of strainrate	–	s^{-1}
Lower mantle rheology			
A_{diff}	Pre-exponential parameter of diffusion creep	1.3×10^{-16}	$Pa^{-1}\ s^{-1}$
E_{diff}	Activation energy of diffusion creep[b]	2×10^5	$J\ mol^{-1}$
V_{diff}	Activation volume of diffusion creep[b]	1.1×10^{-6}	$m^3\ mol^{-1}$
Other model parameters			
κ	Thermal diffusivity	10^{-6}	$m^2\ s^{-1}$
g	Gravitational acceleration	9.8	$m^2\ s^{-2}$
ρ_0	Reference density	3416	$kg\ m^{-3}$
c_p	Specific heat	1250	$J\ kg^{-1}\ K^{-1}$
α_0	Surface thermal expansivity	3×10^{-5}	K^{-1}
γ_{410}	Clapeyron slope of 410 km phase transition[c]	$1 - 2 \times 10^6$	$Pa\ K^{-1}$
γ_{660}	Clapeyron slope of 660 km phase transition[c]	$(-1.5) - (-2.5) \times 10^6$	$Pa\ K^{-1}$
$\delta_{\rho 410}$	Density contrast of 410 km phase transition[d]	273	$kg\ m^{-3}$
$\delta_{\rho 660}$	Density contrast of 660 km phase transition[d]	341	$kg\ m^{-3}$

[a] Parameters of wet olivine based on Hirth and Kohstedt (2003).
[b] Čížková et al. (2012).
[c] Bina and Helffrich (1994).
[d] Steinbach and Yuen (1995).

where A_{diff} is pre-exponential parameter of diffusion creep, E_{diff} is activation energy of diffusion creep, p is hydrostatic pressure, V_{diff} is activation volume of diffusion creep, R is the gas constant and T is the absolute temperature. Dislocation creep viscosity is defined as:

$$\eta_{disl} = A_{disl}^{-1/n} \quad \dot{\varepsilon}_\parallel^{(1-n)/n} \quad exp\left(\frac{E_{disl} + pV_{disl}}{nRT}\right) \quad . \tag{2}$$

Here A_{disl}, E_{disl} and V_{disl} are pre-exponential parameter, activation energy and activation volume of dislocation creep, $\dot{\varepsilon}_\parallel$ is the second invariant of the strain rate tensor and the exponent $n = 3.5$ (Kameyama et al., 1999). Finally the power-law stress limiter viscosity is formulated as:

$$\eta_y = \sigma_y \dot{\varepsilon}_y^{-(1/n_y)} \quad \dot{\varepsilon}_\parallel^{(1/n_y)-1} \tag{3}$$

where $\dot{\varepsilon}_y$ is a reference strain rate and σ_y is the corresponding stress limit. The exponent n_y is usually taken within the range of 5–10, here we apply $n_y = 10$. The stress limit is based on stress estimates in the subducting

slab. Values are usually in the range of $0.1 - 1$ GPa. Here we mostly use $\sigma_y = 0.2$ GPa, but some tests are also performed for $\sigma_y = 0.5$ GPa. Parameters of the above mechanisms are based on experiments on olivine (Hirth and Kohlstedt, 2003) and are specified in Table 1. Viscosities of individual creep mechanisms are combined into an effective viscosity as

$$\frac{1}{\eta_{eff}} = \frac{1}{\eta_{diff}} + \frac{1}{\eta_{disl}} + \frac{1}{\eta_y} + \frac{1}{\eta_{max}}, \tag{4}$$

where the maximum cut-off viscosity $\eta_{max} = 10^{29}$ Pa s. In the lower mantle the deformation is assumed to be predominantly through diffusion creep (Karato et al., 1995). We therefore take $\eta_{eff} = \eta_{diff}$ in the lower mantle with parameters based on slab sinking speed analysis (Čížková et al., 2012). The viscosity increase at 660-km interface $\Delta\eta_{660} \sim 20$ (Fig. 1c).

The primary focus of the present paper is to demonstrate the effects of rheological description of the decoupling crust. To that end we perform numerical experiments in two groups of models. For reference we first run numerical experiments in a series of models with a constant crustal viscosity and we vary both the thickness of the crustal layer and its viscosity. Crustal material is prescribed in a layer of constant thickness positioned along the surface of the subducting plate and along an arc that separates the subducting and overriding plates. We test three initial thicknesses of this compositionally different material (7, 10 and 15 km) and three values of its constant viscosity 10^{20}, 5×10^{20} and 10^{21} Pa s. In this group of 9 models we evaluate the combined effects of the crustal viscosity and thickness on the slab deformation and its ability to penetrate the lower mantle. Sandiford and Moresi (2019) have demonstrated that the thickness of the weak decoupling layer varies during the slab evolution, it is therefore problematic to use the initial thickness of the compositionally different crust as a measure of the weak layer. Furthermore, in order to obtain viscosity in the vicinity of the boundary between the crustal and lithospheric material, we apply harmonic averaging of their viscosities weighted with the volume fraction of crustal/mantle material. This averaging prefers lower (crustal) viscosity and thus effectively makes the decoupling (low viscosity) layer thicker than is the layer of the compositionally distinct crustal material. Therefore we will refer to the thickness of the model crust as 'thin', 'intermediate' and 'thick' and we will report time variations of its effective thicknes d_{cr}^{eff} measured during the calculation (the thickness of the low viscosity channel at the depth of 40 km taken perpendicular to the slab direction).

The main focus of this paper are the models of the second group. In these models the crustal layer has a composite nonlinear rheology that combines dislocation creep (Ranalli, 1995) and a Byerlee type deformation component (Karato, 2008) as an approximation of brittle failure, further referred to as pseudoplastic deformation. Similarly to mantle material (Eq. (2) above), dislocation creep viscosity is defined as

$$\eta_{disl}^c = A_c^{-1/n_c} \quad \dot{\varepsilon}_\parallel^{(1-n_c)/n_c} \quad exp\left(\frac{E_c + pV_c}{n_c RT}\right) \quad . \tag{5}$$

Here A_c, n_c, E_c and V_c are pre-exponential parameter, exponent, activation energy and activation volume of the dislocation creep in the crust. Pseudoplastic deformation is defined by the viscosity component η_{pl}:

$$\eta_{pl} = \frac{\sigma_y^c}{2\dot{\varepsilon}_\parallel} \quad , \tag{6}$$

where σ_y^c is stress limit in the crust. This stress limit σ_y^c increases with lithostatic pressure as

$$\sigma_y^c = \tau_c + \mu p \quad . \tag{7}$$

Here τ_c is the cohesion and μ friction coefficient. Crustal effective viscosity is then calculated as

$$\frac{1}{\eta_{eff}^c} = \frac{1}{\eta_{disl}^c} + \frac{1}{\eta_{pl}} \tag{8}$$

Parameters of both deformation mechanisms are given in Table 2. In order to assess the sensitivity of the results to parameter choice, we evaluate several models. In the reference model PwlM1 the parameters of both dislocation creep and pseudoplastic deformation are based on experiments on quartzite (Liao et al., 2017; Ranalli, 1995). Models PwlM2 and PwlM3 have modified parameters of the pseudoplastic deformation (see Table 2) and yield lower and higher viscosities η_{pl} than the reference model. The influence of the dislocation creep parameters was further tested in model PwlM4 where we used dislocation creep parameters based on the experiments on diabase (Shelton and Tullis, 1981) which is compositionally equivalent to volcanic basalt or plutonic gabbros present in the oceanic crust. All model experiments with the nonlinear crustal model were carried out with intermediate crustal

Table 2
Models with nonlinear crustal rheology.

Symbol	Meaning	PwlM1	PwlM2	PwlM3	Units
A_c	Pre-exponential parameter of dislocation creep	2.5×10^{-17}	2.5×10^{-17}	2.5×10^{-17}	$Pa^{-1} \ s^{-1}$
E_c	Activation energy of dislocation creep	1.54×10^5	1.54×10^5	1.54×10^5	$J \ mol^{-1}$
V_c	Activation volume of dislocation creep	0	0	0	$m^3 \ mol^{-1}$
n_c	dislocation creep exponent	2.3	2.3	2.3	–
τ_c	Cohesion	1×10^7	0.5×10^7	2×10^7	Pa
μ_c	Friction coefficient	0.1	0.05	0.2	–
γ_{410}	Clapeyron slope 410 km phase transition	2	2	2	MPa/K
γ_{660}	Clapeyron slope 660 km phase transition	−2.5	−2.5	−2.5	MPa/K

		PwlM4	PwlM1_0PT	PwlM1_660	Units
A_c	Pre-exponential parameter of dislocation creep	8.8×10^{-25}	2.5×10^{-17}	2.5×10^{-17}	$Pa^{-1} \ s^{-1}$
E_c	Activation energy of dislocation creep	2.6×10^5	1.54×10^5	1.54×10^5	$J \ mol^{-1}$
V_c	Activation volume of dislocation creep	10	0	0	$m^3 \ mol^{-1}$
n_c	dislocation creep exponent	3.4	2.3	2.3	–
τ_c	Cohesion	2×10^7	1×10^7	1×10^7	Pa
μ_c	Friction coefficient	0.2	0.1	0.1	–
γ_{410}	Clapeyron slope 410 km phase transition	2	0	0	MPa/K
γ_{660}	Clapeyron slope 660 km phase transition	−2.5	0	−2.5	MPa/K

thickness and mantle material yield stress σ_y (Eq.(3)) of 0.2 GPa.

4. Results

4.1. Constant viscosity crust

Previous work has shown that a constant viscosity of the crust has a significant influence on the velocity of the subducting plate (Androvičová et al., 2013) and also on its deformation in the transition zone and ability to penetrate the lower mantle (Čížková and Bina, 2013; Goes et al., 2017; Čížková and Bina, 2019). In the first group of our experiments we will further evaluate the combined effects of crustal thickness and its (constant) viscosity. We will demonstrate a trade-off between these two parameters. To that end we performed nine model runs with three different values of constant crustal viscosity 10^{20}, 5×10^{20} and 10^{21} Pa s and three values of initial crustal thickness - 7, 10 and 15 km (refered to as thin, intermediate and thick further on). The stress limit of the mantle material was 0.2 GPa in these experiments. For all models from this group we used the same values of Clapeyron slopes ($\gamma_{410} = 2$MPa/K and $\gamma_{660} = -2.5$MPa/K).

Evolution of two models - with weak (10^{20} Pas) and strong (10^{21} Pas) crust - is shown in Fig. 2. Both models have intermediate crustal thickness. Panels 2a-2c show three snapshots that illustrate the model with weak crust. It reaches the endothermic phase boundary at 660-km depth after 4 Ma evolution from the initial state (Fig. 2a). Slab material in the transition zone squeezed between the extra negative buoyancy of the 410-km elevation and positive buoyancy of the depressed 660-km phase transition is weakened thanks to the nonlinear mantle rheology and forms a first buckle. After that the slab buckles quasiperiodically and remains stagnant in the transition zone (Fig. 2bc). During buckling, the slab oscillates between stages of fast rollback (3–5 cm/year) when new

buckles start and stages of limited or no rollback while buckles are being tightened when the bottom of buckle approaches the 660-km boundary (Čížková and Bina, 2013). Slab dip angle oscillates between the values of ~30 deg. and 70 deg. (Fig. 3, solid red line), low dip angle being associated with faster trench rollback and vice versa (cf. Fig. 3, solid black line). The model with a strong crust (Fig. 2d-f) results in much slower rollback (0.5–1 cm/year, Fig. 3 dashed black line) and penetrative slab. Here higher crustal viscosity causes higher friction near the contact of the subducting and overriding plates and slab rotates towards vertical, displaying significantly higher dip angles (50–90 deg., Fig. 3 dashed red line). The slab thus buckles largely vertically showing limited rollback (Čížková and Bina, 2013; Goes et al., 2017).

In Fig. 4 we compare all models with constant crustal viscosity. We show here a single snapshot of viscosity for each model. This snapshot is taken at the moment when a 2500 km long part of the slab has been subducted. By comparing these snapshots we can conclude that increasing of the crustal thickness has a similar effect as decreasing the crustal viscosity. Models with efficient crustal decoupling (either through higher crustal thickness or lower crustal viscosity) result in stagnation at 660 km depth while models with less efficient decoupling have penetrating slabs. These observations illustrate a trade off between the viscosity of the weak crustal layer and its thickness.

4.2. Nonlinear crustal rheology

In our second group of experiments we prescribe a more realistic, composite nonlinear rheology in the crustal layer with a combination of dislocation creep and pseudoplastic deformation. First, we will demonstrate the time evolution of a model with dislocation creep and pseudoplastic parameters based on Ranalli (1995) as implemented in the upper crust by Liao et al. (2017). We will further denote this model PwlM1 as the reference model case. Fig. 5 shows 6 snapshots of the evolution of this reference model. After approximately 5 Ma of subduction, the slab tip reaches the phase boundary at 410 km and is accelerated by the extra negative buoyancy exerted by the exothermic phase transition (cf. black line in Fig. 6a). Consequently, the strainrate within the crustal channel increases and that reduces crustal viscosity (see associated local minimum of average crustal viscosity in Fig. 6a, red line). Maximum plate velocity during this accelerating phase reaches as high as 130 cm/year, though only for a very short period of 1 Ma. The slab tip promptly approaches the 660 km boundary and simultaneously plate velocity decreases steeply due to the combined effects of the endothermic phase transition and viscous resistance of the stiffer lower mantle. Strainrate in the crustal channel decreases and the average crustal viscosity increases. The slab arrives at the 660 km phase boundary under a steep angle close to the vertical and develops a backward deflection. Stresses exerted by extra buoyancy due to both
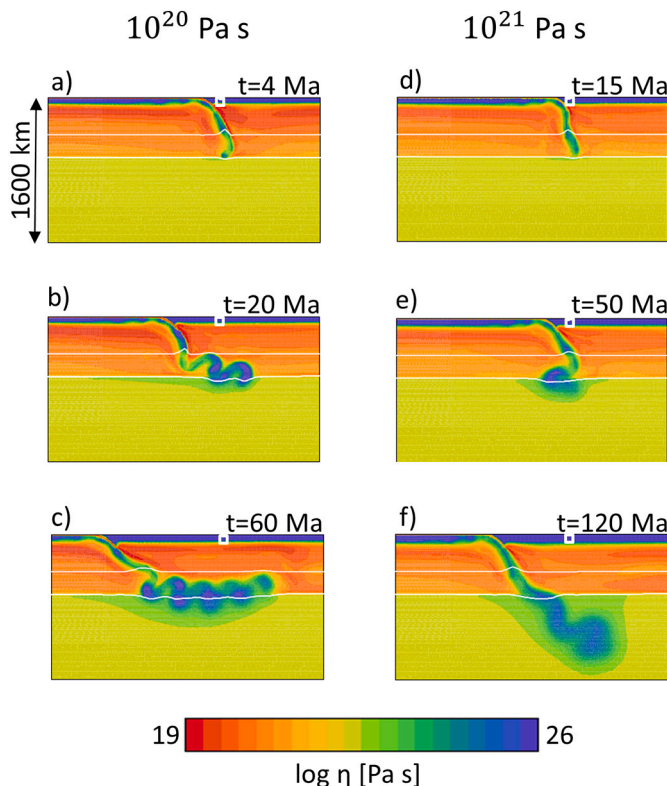
10^{20} Pa s 10^{21} Pa s

Fig. 2. Zoomed-in plots showing time evolution of viscosity in the 3000 km wide and 1600 km deep window for models with low viscosity crust of 10^{20} Pa s (a-c) and for high viscosity crust of 10^{21} Pa s (d-f). Both models have intermediate-thick crust. White lines indicate positions of the phase transitions at 410-km and 660-km depths.
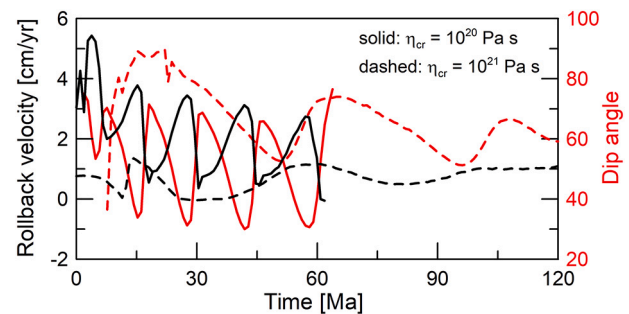
Fig. 3. Time evolution of rollback velocity (black lines) and slab dip angle in the depth interval 200–300 km (red lines) for two models with intermediate crustal thickness. Solid lines are for the model with weak crust (10^{20} Pa s) and dashed lines for the model with strong crust (10^{21} Pa s). (For interpretation of the references to color in this figure legend, the reader is referred to the web version of this article.)
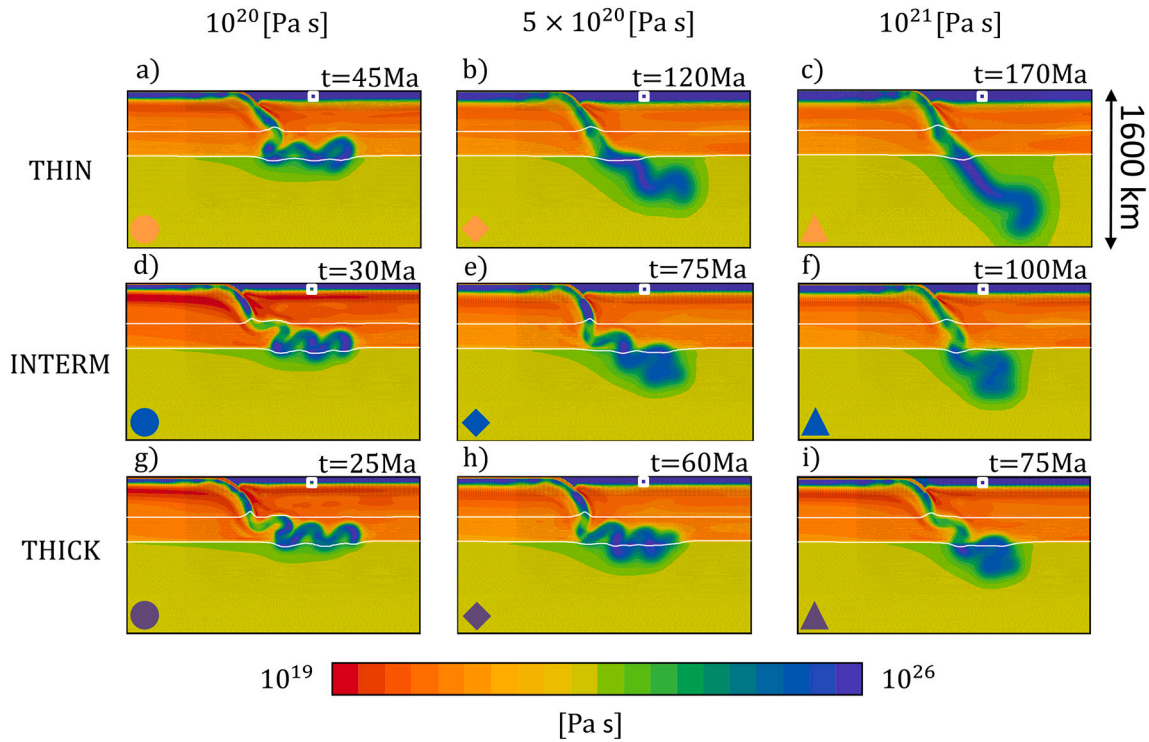
Fig. 4. Zoomed-in plots showing 3000 km wide and 1600 km deep window for models with three different crustal thickness and viscosity values. Snapshot is taken at the moment when a 2500 km long part of the slab has been subducted. Panels a, b and c show models with thin crust, panels d, e and f represent intermediate crust thickness models and panels g, h and i have show models with thick crust. Left column (panels a, d, g) shows models with the low crustal viscosity of 10^{20} Pa s, middle column (panels b, e, h) is for models with intermediate crustal viscosity of 5×10^{20} Pa s and right column (panels c, f, i) represents models with the strong crust with viscosity 10^{21} Pa s. White lines indicate positions of the phase transitions at 410 and 660 km depth. White squares mark the initial position of the trench. Symbols in the lower-left corner represent each model in Fig. 11.
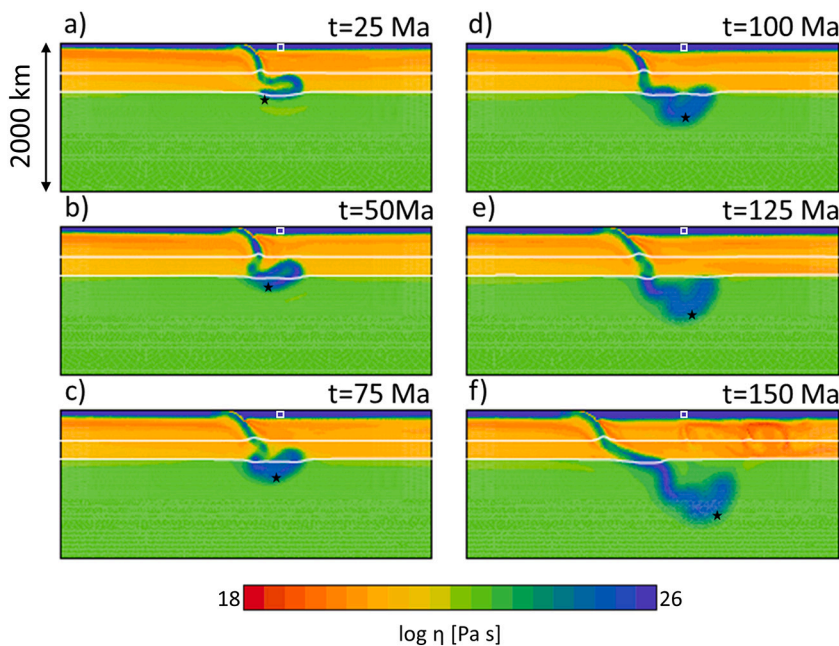
Fig. 5. Reference model PwlM1 with nonlinear crustal rheology (combination of dislocation creep and pseudoplastic deformation). Thickness of the crust is 10 km. Part of the model domain, 2000 km deep and 3000 km wide, is shown. Six snapshots of viscosity are shown with a timestep of 25 Ma. White lines indicate position of the phase transitions at 410 and 660 km depth. White square marks initial position of the trench. Black stars indicate the position of the tracer used for determining the penetration depth.

phase transitions weaken the slab in the transition zone and the first buckle forms at ~12 Ma (see associated local increase of plate velocity on the black line in Fig. 6a). Second buckle starts to develop at about 40 Ma while the accumulated slab material is slowly sinking through the 660 km phase boundary into the lower mantle. At about 70–80 Ma another buckle develops which produces another local maximum in the

plate velocity curve and corresponding decrease in the crustal viscosity. The slab, which was initially temporarily stagnant around 30–40 Ma changes thereafter into a penetrative mode.

Slab dip evolution in model PwlM1 is shown in Fig. 6b (red line) together with the rollback velocity (black line). In the early stages of subduction the low dip-angle is associated with rollback episodes and
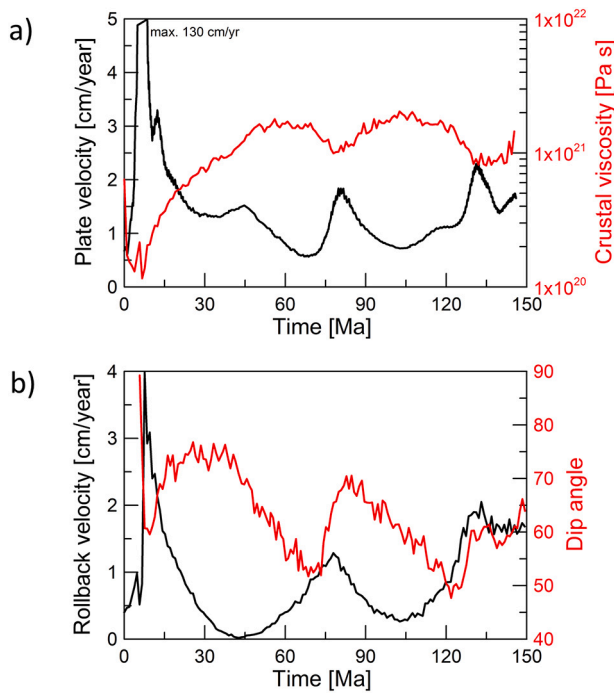
Fig. 6. Time development of some characteristics of the model PwlM1. a) plate velocity and average crustal viscosity, b) rollback velocity and slab dip angle in the depth interval 200–300 km.

subhorizontal buckling at the 660-km boundary. In later stages the anticorrelation between shallow slab dip angle and rollback disappears as rollback is no more controlled by slab deformation in the upper mantle and transition zone. It is increasingly affected by the large scale return flow from the lower mantle. At ~120 Ma the flat-lying part of the slab makes its way through the endothermic phase boundary and starts its decsent through the lower mantle. At that time the dip angle is 60 deg. and trench rolls back with 2 cm/year.

4.2.1. Variations of crustal rheological parameters

Further we will assess the sensitivity of the system to the variations in crustal rheological parameters. First we will vary the pseudoplastic rheology. In case of model PwlM2 with twice lower cohesion and pressure gradient μ (Fig. 7ab) the crustal viscosity is lower at the very

beginning of the subduction process (cf. green and black lines in Fig. 8b, first ~5Ma). It results in higher plate velocity (Fig. 8a, green line), than in reference model PwlM1 (cf. Fig. 8a, black line). The first maximum corresponding to the acceleration due to the 410-km exothermic phase transition reaches an extreme value of 250 cm/year and also the secondary and tertiary maxima attained at 53 Ma and 103 Ma during forming of the subsequent buckles are significantly higher than in the reference case (4 cm/year and 2.8 cm/year compared to 2 cm/year in the reference case). The slab rolls back and stagnates at the endothermic phase transition at 660 km depth (Fig. 7ab). On the other hand, higher pseudoplastic stress limit entailed by twice higher cohesion and pressure gradient μ in model PwlM3 (Fig. 7 cd) causes higher crustal viscosity in shallow parts of the crust. Due to the higher crustal viscosity it is harder for the plates to decouple. It implies lower plate velocity (Fig. 8a) and steeper dip angle as the (slow) slab is rotating towards the vertical in the shallow upper mantle and consequently the rollback is significantly reduced with respect to the reference model PwlM1 and the slab penetrates the lower mantle. We should note here a seemingly counterintuitive behavior of crustal viscosities in models PwlM1 - PwlM3 with variable crustal strength as illustrated in Fig. 8b. One may expect that model PwlM3 should exhibit higher crustal viscosities then the other two models, while the opposite situation is observed e.g.~30 Ma. This comparison just illustrates that it is necessary to view these processes as strongly nonlinear and time dependent. The minimum in model PwlM3 at ~30 Ma corresponds to the moment when the slab crosses the 410-km phase transition and accelerates. This crossing of 410-km occured much later than in models PwlM1 and PwlM2, because the crustal viscosity at the beginning of slab descent in PwlM3 is higher and the slab is consequently slower in the first 30 Ma (cf. Fig. 8a). The general trend of the three curves presented in Fig. 8b however reflects the fact that viscosity in model PwlM3 is higher than in PwlM1 which is still stronger than PwlM2.

We have also investigated the effect of varying the parameters of the dislocation creep. To that end we executed model PwlM4 with pseudoplastic parameters identical to model PwlM3 and with parameters of dislocation creep based on Shelton and Tullis (1981). We did not notice significant difference in character of subducting slab behavior between these two models PwlM3 and PwlM4. We therefore conclude that pseudoplastic deformation as a dominant deformation mechanism in shallow part of the slab (see Fig. 9) has a stronger influence on slab behavior than the parameters of dislocation creep.
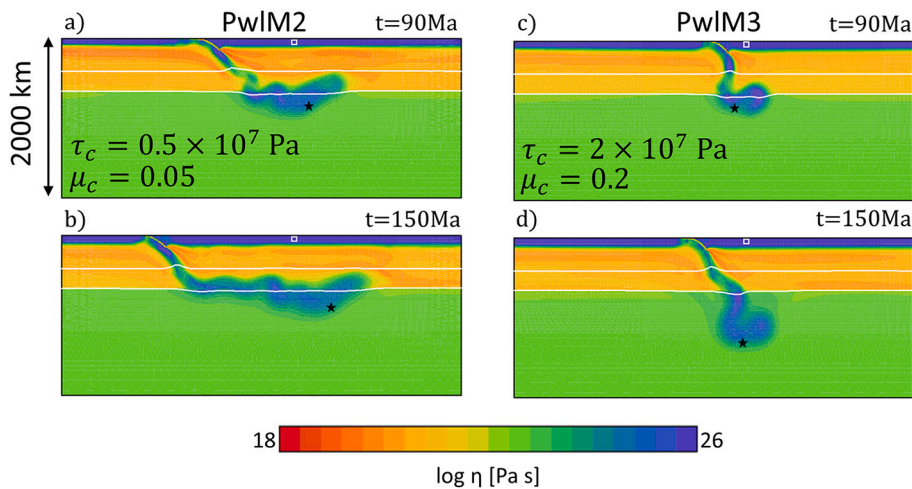
Fig. 7. Two snapshots of viscosity in model PwlM2 (a,b) and PwlM3 (c,d). Zoom of the model domain 2000 km deep and 3000 km wide. White lines indicate positions of the phase transitions at 410 and 660 km depth. White square marks initial position of the trench. Black stars indicate the position of the lowest tracer used for determining the penetration depth.
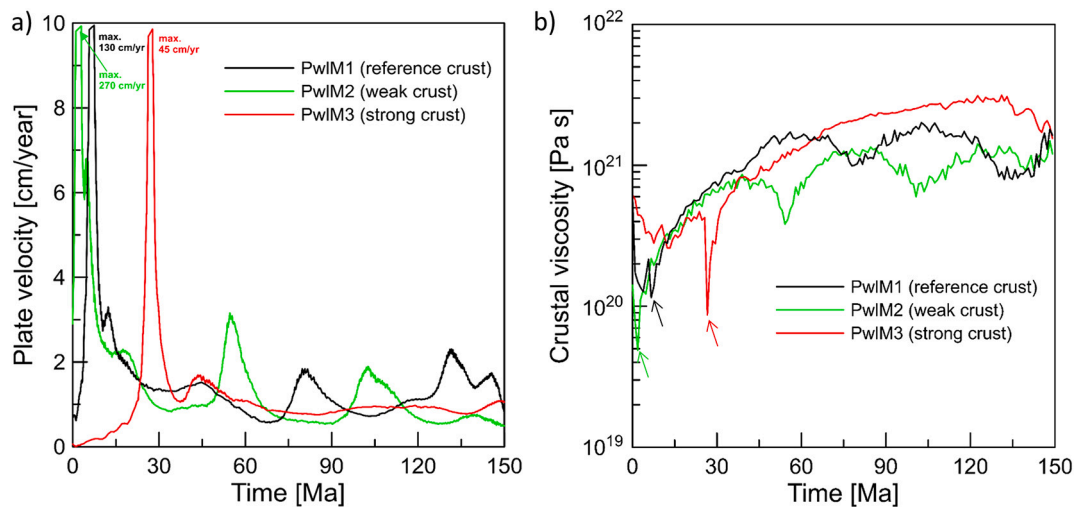
Fig. 8. Time evolution of the plate velocity in models PwlM1 (black line), PwlM2 (green line) and PwlM3 (red line). Plate velocity is measured in subcrustal lithosphere 2000 km to the right from the left-hand-side ridge. Maximum value of plate velocity in the moment of acceleration by the exothermic phase transition of 410 km depth is 250 cm/year for PwlM2 model, 130 cm/year for the PwlM1 and 45 cm/year for the PwlM3 model. b) Time evolution of the crustal average viscosity in the same models. Color arrows indicate minimum of viscosity corespondig to the maximum of velocity as indicated on Fig. 8a. (For interpretation of the references to color in this figure legend, the reader is referred to the web version of this article.)
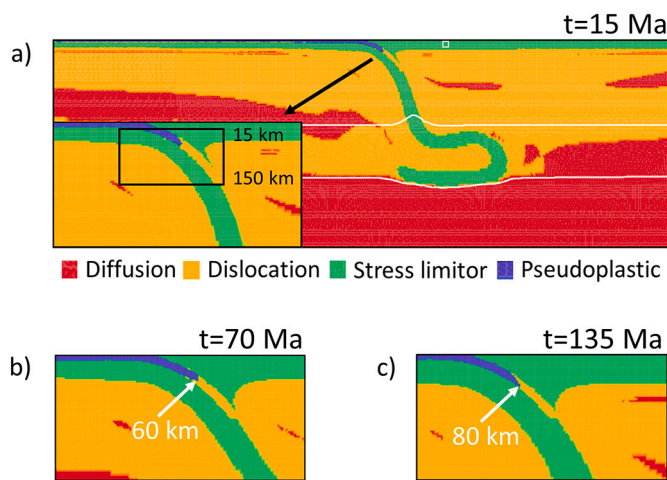
Fig. 9. Dominant deformation mechanism in model PwlM1, time $t = 15$ Ma. Blue color indicates pseudoplastic deformation, green color stress limiter, yellow dislocation creep and red is for diffusion creep. We show part of the model domain, 1000 km deep and 3000 km wide. White lines indicate positions of the phase transitions at 410 and 660 km depth. The white square marks the initial position of the trench. Closeup in the lower left corner shows the detail of the contact of the plates 300 km deep and 600 km wide. Black rectangle marks the depth range used for calculations of the average crustal viscosity. b) Detail of the plates contact at 70 Ma. White arrow marks the transition between pseudoplastic deformation dominated and dislocation creep dominated areas in the crust. Horizontal velocity of the plate is 0.6 cm/year and mean strainrate in the crust is $1.9 \times 10^{-14} s^{-1}$. c) The same as b), but for 135 Ma. Horizontal velocity of the plate is 1.95 cm/year and mean strainrate in the crust is $5.8 \times 10^{-14} s^{-1}$. (For interpretation of the references to color in this figure legend, the reader is referred to the web version of this article.)

4.2.2. Effects of phase transition parameters

Finally we have tested the influence of the strength of the phase transitions on the slab behavior. Fig. 10 shows snapshots taken at 120 Ma for four models with contrasting Clapeyron slopes of both major phase transitions $\gamma_{410}(1 \text{MPa/K}, 2 \text{MPa/K})$ and $\gamma_{660}(-1.5 \text{MPa/K}, -2.5 \text{MPa/K})$. Other (rheology) parameters remain the same as in model PwlM1. Fig. 10a presents the snapshot of model PwlM1 with

reference Clapeyron slopes ($\gamma_{410} = 2 \text{MPa/K}$ and $\gamma_{660} = -2.5 \text{MPa/K}$). At 120 Ma the slab has rolled back by ~ 800 km and after temporary stagnation at 660 km depth has already started to penetrate the lower mantle. In case of the lower value of the Clapeyron slope of the endothermic phase transition at 660 km depth (Fig. 10b), slab mobility is increased with respect to the reference model due to the lower resistance of the endothermic phase transition. This results in faster subduction, faster rollback and deeper penetration of the slab. On the other hand, if we decrease the Clapeyron slope of the exothermic transition at 410 km depth while keeping the higher (reference) Clapeyron slope of the 660 km phase transition (Fig. 10c) the subducting plate has slightly faster rollback than in the reference model PwlM1 and less penetration to the lower mantle. It also exhibits less buckling due to reduced stress exerted by the petrological buoyancy anomalies associated with both phase transitions on the slab in the transition zone. Finally if both Clapeyron slopes are reduced (Fig. 10d) the slab penetrates the lower mantle while still experiencing fast rollback. Low Clapeyron slope of the 410 km phase transition results in negligible buckling.

5. Discussion

In numerical modeling of subduction an entrained weak layer is widely used to decouple the subducting and overriding plate (Sandiford and Moresi, 2019) with either constant viscosity (e.g. Běhounková and Čížková, 2008; Chertova et al., 2012; Holt et al., 2015; Agrusta et al., 2017; Briaud et al., 2019) or nonlinear rheology (e.g. Crameri and Tackley, 2014; Garel et al., 2014; Liao et al., 2017; Li et al., 2019). The magnitude of crustal viscosity was reported to affect plate velocities (Androvičová et al., 2013; Holt et al., 2015) and higher crustal viscosity inhibits rollback (Čížková and Bina, 2013; Arredondo and Billen, 2017; Holt et al., 2015). Consequently, also the deeper deformation of subducted slabs and slab potential stagnation at the base of the upper mantle is strongly sensitive to the decoupling of the subducting and overriding plates. While low (constant) viscosity of the crust results in fast rollback and stagnation, strong crust results in reduced rollback and easier penetration to the lower mantle (e.g. Čížková and Bina, 2013; Goes et al., 2017; Čížková and Bina, 2019). Despite that, numerical modeling studies seldom pay attention to an explicit discussion of the effects of weak crustal layer parameterisations. Sandiford and Moresi (2019) have recently shown that the lubrication effect of the weak crustal layer is further affected by its thickness which evolves with time
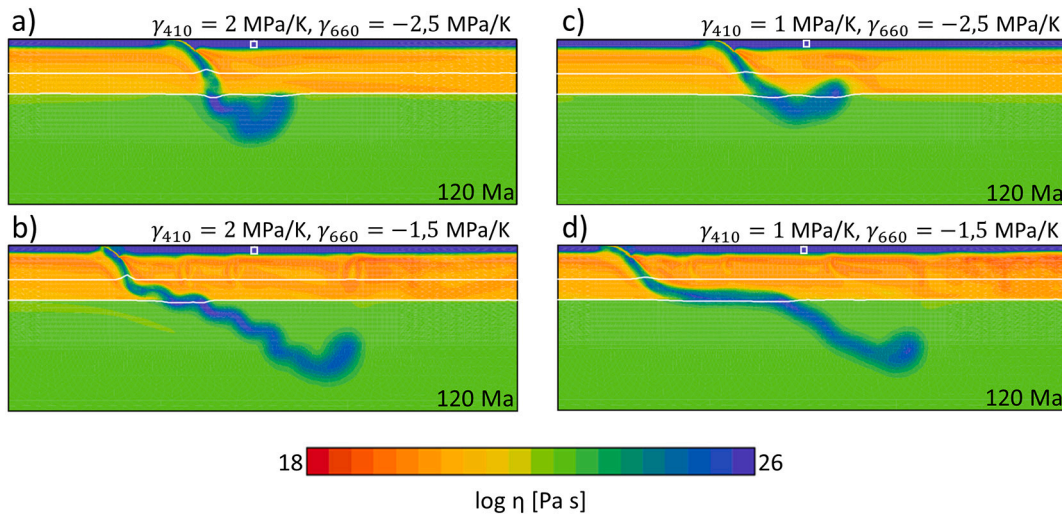
Fig. 10. One snapshot at 120 Ma of viscosity in four models with varying Clapeyron slopes of 410 km and 660 km phase transitions. Reference nonlinear crustal rheology is used. Part of the model domain 2000 km deep and 6000 km wide is shown. White lines indicate positions of the phase transitions at 410 and 660 km depth. White square marks initial position of the trench.

in the models with constant viscosity crust. They demonstrated that transient thinning of the crust may hamper lubrication if the temporarily thinned layer is not properly resolved. Here we conducted an analysis of the combined effects of the crustal thickness and crustal viscosity magnitude and mainly of its nonlinear rheological description and we investigated the effects on slab velocity, rollback and stagnation in the transition zone.

5.1. Effects of crustal resistance to slab penetration

5.1.1. Models with constant viscosity crust

Models with constant crustal viscosity show that the lubricating effect of the weak crust is dependent both on crustal thickness and magnitude of its viscosity and that increasing crustal thickness has the same effect as decreasing its viscosity. This can be quantified by a frictional resistance parameter R that we introduce as the ratio of the viscosity over the effective thickness of the weak crustal layer $R = \frac{\eta_{cr}}{d_{cr}^{eff}}$.

Thickness of the weak decoupling crustal layer varies between 6 km and 18 km over the time span of the model calculation in the models with thin crust. The average values of d_{cr}^{eff} used for resistance calculations are 13–14 km for the three models with $\eta_{cr} = 10^{20} - 10^{21}$ Pa s. For intermediate crustal thickness models the average d_{cr}^{eff} is 16–19 km and for thick crust models it is 23–26 km. The resistance characterises the efficiency of the decoupling - low resistance (weak and/or thick decoupling layer) means well decoupled plates white high resistance (strong and/or thin decoupling layer) is in models with strong coupling of the plates. In Fig. 11 we plot the resistance against the penetration depth of the slab after 150 Ma in order to quantify the penetrative vs. stagnant slab behavior. Each model is represented by one symbol - yellow symbols are for thin crust, blue for intermediate and violet symbols are for thick crust, circles are for models with weak crust, diamonds for intermediate crustal viscosity and triangles for strong crust. The symbols representing stagnant slabs correspond to pentration depths in the shallow lower mantle close to the 660 km boundary, while penetrating slabs will be found deeper in the lower mantle. The transition between stagnant and penetrative slabs is characterised by a resistance value $R_{crit} \approx 2 - 3 \times 10^{16}$ Pa s m^{-1}. By introducing the resistance parameter we want to emphasize that the decoupling efficiency of the weak layer is not controlled by the layer viscosity alone, but rather by the combination of viscosity and thickness. We should however point out that the threshold resistance R_{crit} that separates longer-term stagnant models from penetrative ones reported above is not unique. As the slab penetration/
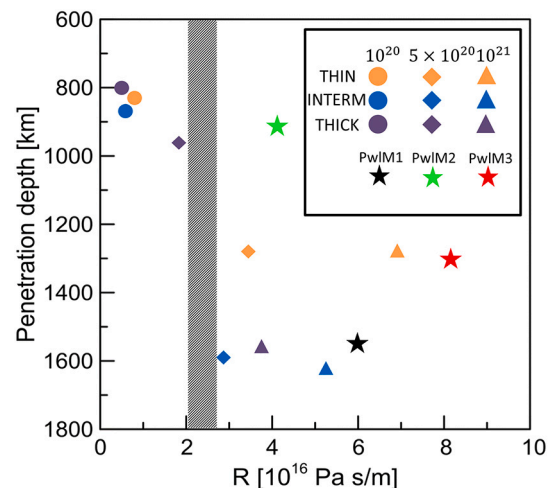
Fig. 11. Penetration depth at 150 Ma as a function of crustal resistance R. R is defined as the ratio between crustal viscosity and its average thickness. Each symbol represents one of the models with constant viscosity crust shown in Fig. 4 (circles, diamonds and triangles) or models with nonlinear crustal rheology (asterisks).

stagnation is influenced by many other model characteristics (apart from the subducting-overriding plates decoupling) the critical resistance may be different for different model parameters such as viscosity jump at 660-km or Clapeyron slope of the endothermic phase transition. For example for models with higher stress limit of 0.5 GPa the character of the slab behavior is similar, but the transition between stagnant and penetrative models occurs at higher value of $R \approx 7 \times 10^{16}$ Pa s m^{-1}.

5.1.2. Models with nonlinear crust

Models with nonlinear crustal rheology show more complicated interaction with the 660-km phase and viscous boundary. The viscosity of the weak decoupling crustal layer is now responding to the slab dynamics and a feedback between the slab velocity and crustal viscosity is observed. Crustal viscosity is anti-correlated with subducting plate velocity - crustal viscosity decreases as the strain-rate increases during slab acceleration, while it increases as the slab slows down and strain-rate is reduced. Both subducting plate velocity and crustal viscosity thus simultaneously reflect the changes in subduction dynamics as slab

interacts with the phase transitions and forms buckles in the transition zone.

Slab rollback is clearly correlated with shallow slab dip angle - low dip angle facilitates rollback (possibly accompanied by subhorizontal buckling) and slab stagnation, while steeply dipping slabs are associated with vertical buckling, show limited rollback and penetrate to the lower mantle. Slab dip angle has been shown to evolve with time and reflect kinematics of the subducting and overriding plates, mantle viscosity and petrological buoyancy of the phase transitions (Cerpa et al., 2014; Yang et al., 2018), but also the crustal viscosity (Čížková and Bina, 2013). Mostly as a result of the forementioned feedback mechanisms average crustal viscosity in our models PwlM1-PwlM3 with nonlinear crustal viscosity varies with time. For the rheological parameters that we used, its variations lie between 5×10^{19} Pa s and 2×10^{21} Pa s. At the beginning, during slab acceleration, the average viscosity of crust in the models PwlM1 and PwlM2 with relatively weak plastic component of crustal rheology is low, so is dip angle and therefore these slabs develop rollback and (temporary) stagnation at 660 km boundary. As the slabs decelerate while interacting with the 660-km boundary, the higher viscosity favours less rollback and strenghtens tendency to penetration. In the model with strong plastic parameters the viscosity is relatively high even in the early stages of subduction and the slab penetrates the lower mantle without a significant stagnation period.

In order to compare the nonlinear crust models with previously discussed models with constant viscosity crust (par. 5.1.1), we tried to evaluate crustal resistance also for models PwlM1-PwlM3. Though it may not necessarily be straightforward that the style of slab deformation should be controlled by the average viscosity within the subduction channel, we may still try and use this average $\eta_{av}(t)$ together with $d_{cr}^{eff}(t)$ to evaluate the resistance $R(t) = \eta_{av}(t)/d_{cr}^{eff}(t)$ as a function of time. Its average values (averaged over 150 Ma subduction evolution) we then plotted in Fig. 11 against the corresponding penetration depths (black, green and red asterisks). Similarly to constant crustal viscosity models, we observe the division between the long-term stagnant model PwlM2 with weak crust that appears in the upper-left part of the graph while the penetrative models PwlM1, PwlM3 with stronger crust are located in the lower-right part of the graph. The division between the stagnant and penetrative models is however shifted towards higher resistance. Apparently the time varying nature of crustal resistance in nonlinear models makes inferences about slab deformation more complicated and using one (average) resistance to characterise the models is problematic.

Stagnation/penetration behavior is therefore further illustrated in Fig. 12 where the penetration depth and sinking velocity are plotted as a function of time. Stagnant slabs are characterised by a penetration depth that remains less than ~800 km in a long term run. An example of a long term stagnant slab is in the model with constant crustal viscosity of 10^{20} Pa s (cf. Fig. 4a). Its penetration depth is in Fig. 12a demonstrated by the blue line and its sinking velocity (Fig. 12b) remains close to zero. For a penetrative slab (e.g. the model with constant crustal viscosity of 10^{21} Pa s presented in Fig. 4c) on the other hand the penetration depth curve does not have a flat part (see Fig. 12a, yellow line) as the slab is descending to the lower mantle without significant hindrance. Its sinking speed (Fig. 12b yellow line) in later stages of slab descent reaches 1 cm/year, which is in agreement with slab sinking speed inferred by van der Meer et al. (2010). The reference model PwlM1 with nonlinear crustal rheology produces the penetration curve somewhere in between (black line in Fig. 12a). It exhibits a flat stagnant part up to approximately 30 Ma and then the penetration depth starts to increase steadily demonstrating the basic characteristic behavior of the reference model with nonlinear crustal rheology.

5.2. Effects of phase transitions in combination with a weak decoupling layer

As discussed above (cf. Fig. 10), the strength of both phase transitions affects slab behavior in the transition zone. In order to isolate the effects of the phase transitions from the effects of nonlinear rheology of the decoupling layer, we investigated five additional models. Three of them are with constant viscosity of crust (10^{20}, 5×10^{20} and 10^{21} Pa s) and without phase transitions. The other two have nonlinear crustal rheology with the same parameters as model PwlM1, but now without phase transitions (PwlM1_0PT) and also the model that has only one phase transition an endothermic one at 660-km depth (PwlM1_660). Fig. 13 shows plate velocities in these models compared with the model PwlM1. Let us start with the models with constant crustal viscosity (blue, orange and purple lines in Fig. 13). At the beginning the slab tip is at the depth of 200 km and it starts to subduct with plate velocity ~1–2 cm/year. As the slab subducts the increasing negative buoyancy anomaly results in increasing plate velocity. In case of the stiff crust ($\eta_{cr} = 10^{21}$ Pa s (purple)) the maximum plate velocity of 4 cm/year is attained at 25 Ma. Weaker crust (blue and orange lines) results in more efficient lubrication and therefore the maxima of plate velocity are reached earlier and the maximum is higher (25 cm/year at 5 Ma in case of the weakest crust with $\eta_{cr} = 10^{20}$ Pa s). At the moment when the slab tip approaches the stiffer lower mantle, it slows down and the plate velocity decreases. Now let us look at the effects of nonlinear crustal
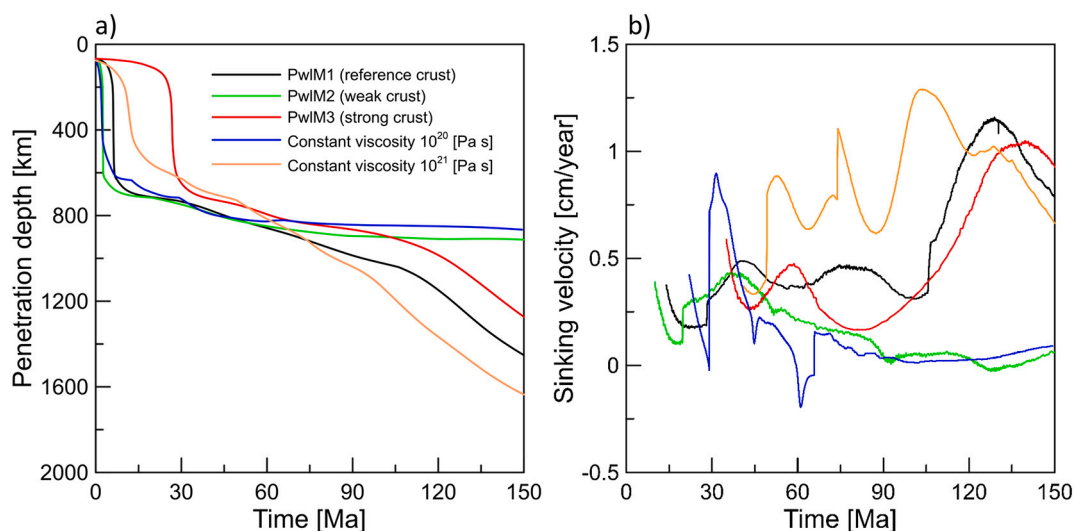
Fig. 12. Panel a): Slab penetration depth monitored by the position of the deepest tracer located in the slab. Panel b): Sinking velocity computed from the position of the deepest tracer located in the slab. The color legend is the same as in panel a).
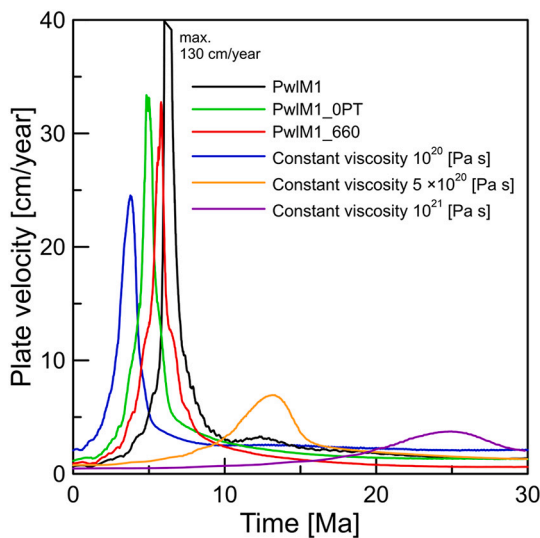
Fig. 13. Time development of the plate velocity in models with reference nonlinear crustal rheology PwlM1. Crust thickness is 10 km, stress limit of 2×10^8 Pa. Black line shows model with both 410 km and 660 km phase transition, green line is for model without phase transitions and red line for model with only 660 km phase transition. For comparison we also show models with constant crustal viscosity of 10^{20} Pa s (blue line), 5×10^{20} Pa s (yellow line) and 10^{21} Pa s (purple line). (For interpretation of the references to color in this figure legend, the reader is referred to the web version of this article.)

viscosity, also in the model without phase transitions (PwlM1_0PT green line in Fig. 13). At the beginning the plate is slower than in the model with constant viscosity 10^{20} Pa s (cf. blue and green lines), because the nonlinear rheology yields higher viscosity at low deformation rates. However, as the slab tip subducts deeper and develops more negative buoyancy, the slab accelerates and ensuing higher velocity and deformation rate results in crustal viscosity reduction. Crustal viscosity then decreases below 10^{20} Pa s and therefore the maximum velocity of 33 cm/year attained in the model PwlM1_0PT is higher than in case with $\eta_{cr} = 10^{20}$ Pa s. Model PwlM1_660 which includes only the endothermic phase transition at 660 km shows a very similar behavior as the model without phase transitions. It is slightly slower from the very beginning, because the 660-km phase boundary exerts a small resistive force to the downwelling mantle material pushed to the lower mantle in front of the downgoing cold slab tip before the tip itself reaches the phase transition. A small difference between the curves with and without the endothermic phase transitions suggests that the primary role is played by the viscous resistance of a strong lower mantle and that the phase transition has only a secondary effect here. On the contrary, adding the exothermic phase transition at 410-km depth (model PwlM1 (black line)) results in a very strong acceleration thanks to the feedback between the slab velocity and crustal viscosity - maximum plate velocity is now 130 cm/year.

Since our mantle material composition is limited to olivin, we use relatively mild values of the Clapeyron slopes of the major phase transitions, as the overall buoyancy effect of the phase transitions in the pyrolitic mantle should be significantly reduced with respect to pure olivine composition (Arredondo and Billen, 2016). Even then we obtain a very strong slab acceleration when its tip first encounters the 410-km phase transition. Extremely high plate velocity maximum (more than 1 m/yr in case of a reference plasticity parameterisation) is only attained in a very short time interval. Moreover we have to keep in mind that here we probably encounter one of the limitations of a 2D model setup. The slab tip crosses the 410-km boundary at the same moment along its whole (infinite) length. In real world this effect will always be smaller as a 3D plate will be passing through the phase boundary gradually, so the acceleration will be significantly smaller.

5.3. Deformation partitioning in the weak layer between pseudo-plastic and dislocation creep

As discussed in Section 4.2.1, slab behavior is strongly sensitive to the variations of parameters of pseudoplastic deformation that dominates at shallow depths (Fig. 9a). Our pseudoplastic deformation approximates brittle failure which should dominate at low temperature and high strainrate. As both temperaure and strainrate within crustal channel vary with time during slab evolution one may expect that the transition between brittle (pseudoplastic) and ductile (dislocation creep) deformation will also develop in time. The average transition depth between the Byerlee type pseudoplastic deformation and viscous dislocation creep in our reference model PwlM1 is ∼ 60 km during the subduction evolution. During slab acceleration periods, when crustal viscosity decreases and plate velocity and strainrate increase, the pseudoplastic deformation dominates up to larger depths of ∼ 80 km. This is illustrated in Fig. 9bc, where the transition depth between pseudoplastic deformation and dislocation creep is marked for two snapshots - at 70 Ma when the plate velocity is 0.6 cm/year (cf. Fig. 8a, black line) and at 135 Ma when plate velocity reaches local maximum of 1.95 cm/year. The shift of the transition depth from 60 km to 80 km during slab acceleration at 135 Ma illustrates its strainrate dependence. One should also note that at 135 Ma (Fig. 9c) the boundary between brittle deformation dominated and ductile deformation dominated areas is tilted, with dislocation creep dominating in the right half of the crustal chanel. This is probably due to the increased temperature near the boundary between the subducting and overriding plates. During slab acceleration the contact zone of the plates is heated by viscous dissipation and temperature in the right half of the crustal channel is by 50 K warmer than the minimum temperature in the slab center (450 K).

5.4. Concluding remarks

The decoupling between the subducting and overriding plates is one of the factors that have strong influence on the slab interaction with the transition zone. The style of deformation, stagnation or lower mantle penetration, appears to be a treshold phenomenon and a small change of other model parameters, e.g. shifting the viscosity transition between the upper and lower mantle to 1000 km depth (Čížková and Bina, 2019), can change the slab behavior from stagnant to penetrative. From that perspective our analysis of the effects of nonlinear crustal rheology shows the situation to be even more complex, since the feedback between the (time variable) crustal viscosity and slab velocity further complicates the subtle balance of thermal and petrological buoyancy that controls slab penetration. The decoupling effects of the (wet) crustal material that in natural subduction zones occur on very fine spatial scales were investigated in terms of reginal scale models focused on the subduction process at shallow depths (e.g. Gerya and Meilick, 2010). Our crust parameterisation does not take into account fine and complex substructure of the crust with a fine sedimental layer at the top underlayed with pillow basaltic lavas, sheeted dike complex and gabro cumulates. Such complex structure is at present beyond the reach of our whole mantle scale models, where resolving crustal structures on kilometer scales remains a challenge. It is therefore difficult to make definitive conclusions about slab stagnation/penetration on the basis of our models. We do however stress the fact that nonlinear crustal rheology strenghtens transient behavior of the subducting slabs and enforces slab penetration after transient period of stagnation. This is probably a more realistic scenario of slab interaction with the transition zone, because in real world observations (mapped by seismic tomography) we do not observe very long term stagnant slabs as are predicted by the models with a low crustal viscosity. In various subduction regions a temporary stagnation is observed (e.g. Japan, Izu-Bonin, Tonga), sometimes followed by penetration (van der Meer et al., 2018). The lateral extent of flat lying part is however typically limited to 1000–1500 km (Goes et al., 2017) while our weak crust models report

subhorizontal buckling and stagnation at 660 km for periods of time longer than 100 Ma resulting in flat-lying slab portions of more than 2000 km.

Author statement

Jakub Pokorný: Methodology, Software, Visualization, Writing-Original draft preparation. Hana Čížková: Supervision, Analysis, Writing- Reviewing and Editing. Arie van den Berg: Conceptualization, Analysis.

Declaration of Competing Interest

None.

Acknowledgements

References

Agrusta, R., Van Hunen, J., Goes, S., 2014. The effect of metastable pyroxene on the slab dynamics. Geophys. Res. Lett. 41 (24), 8800–8808. https://doi.org/10.1002/2014GL062159. ISSN 19448007.

Agrusta, R., Goes, S., van Hunen, J., 2017. Subducting-slab transition-zone interaction: stagnation, penetration and mode switches. Earth Planet. Sci. Lett. 464, 10–23. https://doi.org/10.1016/j.epsl.2017.02.005. ISSN 0012821X.

Androvičová, A., Čížková, H., van den Berg, A., 2013. The effects of rheological decoupling on slab deformation in the Earth's upper mantle. Stud. Geophys. Geod. https://doi.org/10.1007/s11200-012-0259-7. ISSN 00393169.

Arcay, D., Tric, E., Doin, M.P., 2005. Numerical simulations of subduction zones. Effect of slab deghydration on the mantle wedge dynamics. Phys. Earth Planet. Inter. 149 (1–2 SPEC. ISS), 133–153. https://doi.org/10.1016/j.pepi.2004.08.020. ISSN 00319201.

Arredondo, K.M., Billen, M.I., 2016. The effects of phase transitions and compositional layering in two-dimensional kinematic models of subduction. J. Geodyn. 100, 159–174. ISSN 0264-3707. oct. https://doi.org/10.1016/J.JOG.2016.05.009.

Arredondo, K., Billen, M., 2017. Coupled effects of phase transitions and rheology in 2D dynamical models of subduction. J. Geophys. Res. Solid Earth 122, 5813–5830. https://doi.org/10.1002/2017JB014374.

Běhounková, M., Čížková, H., 2008. Long-wavelength character of subducted slabs in the lower mantle. Earth Planet. Sci. Lett. 275 (1–2), 43–53. https://doi.org/10.1016/j.epsl.2008.07.059. ISSN 0012821X.

Behr, W.M., Becker, T.W., 2018. Sediment control on subduction plate speeds. Earth Planet. Sci. Lett. 502, 166–173.

Bijwaard, H., Spakman, W., Engdahl, E.R., 1998. Closing the gap between regional and global travel time tomography. J. Geophys. Res. Solid Earth 103 (B12), 30055–30078. https://doi.org/10.1029/98JB02467. ISSN 01480227.

Billen, M.I., 2010. Slab dynamics in the transition zone. Phys. Earth Planet. Inter. 183 (1), 296–308. https://doi.org/10.1016/j.pepi.2010.05.005. ISSN 0031–9201. Special Issue on Deep Slab and Mantle Dynamics.

Billen, M.I., Hirth, G., 2007. Rheologic controls on slab dynamics. Geochem. Geophys. Geosyst. 8 (8) https://doi.org/10.1029/2007GC001597. ISSN 15252027.

Bina, C.R., Helffrich, G., 1994. Phase transition clapeyron slopes and transition zone seismic discontinuity topography. J. Geophys. Res. Solid Earth 99 (B8), 15853–15860. https://doi.org/10.1029/94JB00462.

Bina, C.R., Stein, S., Marton, F.C., Ark, E.M.V., 2001. Implications of slab mineralogy for subduction dynamics. Phys. Earth Planet. Inter. 127 (1), 51–66. https://doi.org/10.1016/S0031-9201(01)00221-7. ISSN 0031–9201. Processes and Consequences of Deep Subduction.

Briaud, A., Agrusta, R., Faccenna, C., Funiciello, F., van Hunen, J., 2019. Topographic fingerprint of deep mantle subduction. J. Geophys. Res. Solid Earth 125. https://doi.org/10.1029/2019JB017962.

Cerpa, N., Hassani, R., Gerbault, M., Prevost, J.-H., 2014. A fictious domain method for lithosphere-asthenosphere interaction: application to periodic slab folding in the upper mantle. Geochem. Geophys. Geosyst. 15, 1852–1877. https://doi.org/10.1002/2014GC005241.

Chertova, M.V., Geenen, T., Van Den Berg, A., Spakman, W., 2012. Using open sidewalls for modelling self-consistent lithosphere subduction dynamics. Solid Earth 3 (2), 313–326. https://doi.org/10.5194/se-3-313-2012. ISSN 18699510.

Christensen, U.R., 1996. The influence of trench migration on slab penetration into the lower mantle. Earth Planet. Sci. Lett. 140 (1–4), 27–39. https://doi.org/10.1016/0012-821X(96)00023-4. ISSN 0012821X.

Christensen, U., Yuen, D., 1985. Layered convection induced by phase transitions. J. Geophys. Res. Solid Earth 90 (B12), 10291–10300. https://doi.org/10.1029/JB090iB12p10291.

Čížková, H., Bina, C.R., 2013. Effects of mantle and subduction-interface rheologies on slab stagnation and trench rollback. Earth Planet. Sci. Lett. 379, 95–103. https://doi.org/10.1016/j.epsl.2013.08.011. ISSN 0012821X.

Čížková, H., Bina, C.R., 2019. Linked influences on slab stagnation: interplay between lower mantle viscosity structure, phase transitions, and plate coupling. Earth Planet. Sci. Lett. 509, 88–99. https://doi.org/10.1016/j.epsl.2018.12.027. ISSN 0012821X.

Čížková, H., Van Hunen, J., Van den Berg, A.P., Vlaar, N.J., 2002. The Influence of Rheological Weakening and Yield Stress on the Interaction of Slabs with the 670 Km Discontinuity (ISSN 0012821X).

Čížková, H., van Hunen, J., van den Berg, A., 2007. Stress distribution within subducting slabs and their deformation in the transition zone. Phys. Earth Planet. Inter. 161 (3–4), 202–214. https://doi.org/10.1016/j.pepi.2007.02.002. ISSN 00319201.

Čížková, H., van den Berg, A.P., Spakman, W., Matyska, C., 2012. The viscosity of Earth's lower mantle inferred from sinking speed of subducted lithosphere. Phys. Earth Planet. Inter. 200-201, 56–62. https://doi.org/10.1016/j.pepi.2012.02.010. ISSN 00319201.

Crameri, F., Tackley, P.J., 2014. Spontaneous development of arcuate single-sided subduction in global 3-d mantle convection models with a free surface: Crameri and tackley. J. Geophys. Res. Solid Earth 119, 07. https://doi.org/10.1002/2014JB010939.

Duarte, J.C., Schellart, W.P., Cruden, A.R., 2015. How weak is the subduction zone interface? Geophys. Res. Lett. 42 (8), 2664–2673. https://doi.org/10.1002/2014GL062876. ISSN 19448007.

Faccenda, M., Zilio, L.D., 2017. The role of solid–solid phase transitions in mantle convection. Lithos 268–271, 198–224. https://doi.org/10.1016/j.lithos.2016.11.007. ISSN 0024-4937.

Fukao, Y., Obayashi, M., 2013. Subducted slabs stagnant above, penetrating through, and trapped below the 660 km discontinuity. J. Geophys. Res. Solid Earth 118 (11), 5920–5938. https://doi.org/10.1002/2013JB010466. ISSN 21699356.

Garel, F., Goes, S., Davies, D.R., Davies, J.H., Kramer, S.C., Wilson, C.R., 2014. Interaction of subducted slabs with the mantle transition-zone: a regime diagram from 2-D thermo-mechanical models with a mobile trench and an overriding plate. Geochem. Geophys. Geosyst. 15 (5), 1739–1765. https://doi.org/10.1002/2014GC005257. ISSN 15252027.

Gerya, T., Meilick, F., 2010. Geodynamic regimes of subduction under an active margin: effects of rheological weakening by fluids and melts. J. Metamorph. Geol. 29, 7–31. https://doi.org/10.1111/j.1525-1314.2010.00904.x.

Goes, S., Agrusta, R., van Hunen, J., Garel, F., 2017. Subduction-transition zone interaction: A review. Geosphere 13 (3), 644–664 jun.

Hansen, U., Yuen, D.A., Kroening, S., B, L.T., 1993. Dynamical consequences of depth-dependent thermal expansivity and viscosity on mantle circulations and thermal structure. Phys. Earth Planet. Inter. 77, 205–223.

Hirth, G., Kohlstedt, D., 2003. Rheology of the Upper Mantle and the Mantle Wedge: A View from the Experimentalists, 138. American Geophysical Union Geophysical Monograph Series, Washington DC, pp. 83–105. https://doi.org/10.1029/138GM06.

Holt, A.F., Becker, T.W., Buffett, B.A., 2015. Trench migration and overriding plate stress in dynamic subduction models. Geophys. J. Int. 201 (1), 172–192. https://doi.org/10.1093/gji/ggv011. ISSN 1365246X.

Ita, J., King, S.D., 1994. Sensitivity of convection with an endothermic phase change to the form of governing equations, initial conditions, boundary conditions, and equation of state. J. Geophys. Res. 99 (B8), 15919. ISSN 0148-0227. aug. https://doi.org/10.1029/94JB00852.

Iwamori, H., 2007. Transportation of H2O beneath the Japan arcs and its implications for global water circulation. Chem. Geol. 239 (3–4), 182–198. https://doi.org/10.1016/j.chemgeo.2006.08.011. ISSN 00092541.

Kameyama, M., Yuen, D.A., Karato, S.-I., 1999. Thermal-mechanical effects of low-temperature plasticity (the Peierls mechanism) on the deformation of a viscoelastic shear zone. Earth Planet. Sci. Lett. 168 (1–2), 159–172. ISSN 0012-821X. apr. https://doi.org/10.1016/S0012-821X(99)00040-0.

Karato, S.-i., 2008. Deformation of earth materials. In: An Introduction to the Rheology of Solid Earth, 463.

Karato, S.-i., Zhang, S., Wenk, H.-R., 1995. Superplasticity in Earth's Lower Mantle: Evidence from Seismic Anisotropy and Rock Physics. Science 270 (5235), 458 LP – 461, oct.

Katsura, T., Yokoshi, S., Kawabe, K., Shatskiy, A., Manthilake, M., Zhai, S., Fukui, H., Hegoda, H., Yoshino, T., Yamazaki, D., Matsuzaki, T., Yoneda, A., Ito, E., Sugita, M., Tomioka, N., Hagiya, K., Nozawa, A., Funakoshi, K.-i., 2009. P-v-t relations of mgsio3 perovskite determined by in situ x-ray diffraction using a large-volume high-pressure apparatus. Geophys. Res. Lett. 36, 01. https://doi.org/10.1029/2009GL039318.

Li, Z.-H., Gerya, T., Connolly, J.A., 2019. Variability of subducting slab morphologies in the mantle transition zone: insight from petrological-thermomechanical modeling. Earth Sci. Rev. 196, 102874. https://doi.org/10.1016/j.earscirev.2019.05.018. ISSN 0012-8252.

Liao, J., Gerya, T., Thielmann, M., Webb, A.A.G., Kufner, S.K., Yin, A., 2017. 3D geodynamic models for the development of opposing continental subduction zones: the Hindu Kush–Pamir example. Earth Planet. Sci. Lett. 480, 133–146. https://doi.org/10.1016/j.epsl.2017.10.005. ISSN 0012821X.

Nakao, A., Iwamori, H., Nakakuki, T., 2016. Effects of water transportation on subduction dynamics: roles of viscosity and density reduction. Earth Planet. Sci. Lett. 454, 178–191. https://doi.org/10.1016/j.epsl.2016.08.016. ISSN 0012821X.

Nakao, A., Iwamori, H., Nakakuki, T., Suzuki, Y.J., Nakamura, H., 2018. Roles of hydrous lithospheric mantle in deep water transportation and subduction dynamics.

Geophys. Res. Lett. 45 (11), 5336–5343. https://doi.org/10.1029/2017GL076953. ISSN 19448007.

Ranalli, G., 1995. Rheology of the Earth. Springer Science & Business Media. ISBN 0412546701.

Ribe, N.M., 2010. Bending mechanics and mode selection in free subduction: a thin-sheet analysis. Geophys. J. Int. 180 (2), 559–576. https://doi.org/10.1111/j.1365-246X.2009.04460.x. ISSN 0956-540X.

Sandiford, D., Moresi, L., 2019. Improving subduction interface implementation in dynamic numerical models. Solid Earth 10 (3), 969–985. https://doi.org/10.5194/se-10-969-2019.

Schmeling, H., Monz, R., Rubie, D.C., 1999. The influence of olivine metastability on the dynamics of subduction. Earth Planet. Sci. Lett. 165 (1), 55–66. https://doi.org/10.1016/S0012-821X(98)00249-0. ISSN 0012-821X.

Segal, A., Praagman, N., 2005. The Sepran Fem Package, Technical Report, Ingenieursbureau Sepra.

Shelton, G., Tullis, J., 1981. Experimental flow laws for crustal rocks. EOS Trans. Am. Geophys. Union 62.

Stegman, D., Farrington, R., Capitanio, F., Schellart, W., 2010. A regime diagram for subduction styles from 3-d numerical models of free subduction. Tectonophysics 483 (1), 29–45. https://doi.org/10.1016/j.tecto.2009.08.041. ISSN 0040–1951. Convergent plate margin dynamics: New perspectives from structural geology, geophysics and geodynamic modelling.

Steinbach, V., Yuen, D.A., 1995. The effects of temperature-dependent viscosity on mantle convection with the two major phase transitions. Phys. Earth Planet. Inter. 90 (1), 13–36. https://doi.org/10.1016/0031-9201(95)03018-R. ISSN 0031-9201.

Torii, Y., Yoshioka, S., 2007. Physical conditions producing slab stagnation: constraints of the Clapeyron slope, mantle viscosity, trench retreat, and dip angles. Tectonophysics 445 (3–4), 200–209. https://doi.org/10.1016/j.tecto.2007.08.003. ISSN 00401951.

van den Berg, A.P., Keken, P.E., Yuen, D.A., 1993. The effects of a composite non-Newtonian and Newtonian rheology on mantle convection. Geophys. J. Int. 115 (1), 62–78. ISSN 0956540X. oct. https://doi.org/10.1111/j.1365-246X.1993.tb05588.x.

van den Berg, A., Segal, G., Yuen, D., 2015. Sepran: A versatile finite-element package for a wide variety of problems in geosciences. J. Earth Sci. 26 (1), 89–95. ISSN 1674-487X. 1. https://doi.org/10.1007/s12583-015-0508-0.

van der Meer, D., Spakman, W., van Hinsbergen, D., Amaru, M., Torsvik, T., 2010. Towards absolute plate motions constrained by lower-mantle slab remnants. Nat. Geosci. 3, 36–40. https://doi.org/10.1038/NGEO708.

van der Meer, D.G., van Hinsbergen, D.J., Spakman, W., 2018. Atlas of the underworld: Slab remnants in the mantle, their sinking history, and a new outlook on lower mantle viscosity. Tectonophysics 723, 309–448. https://doi.org/10.1016/j.tecto.2017.10.004. ISSN 0040-1951.

van Hunen, J., van den Berg, A.P., Vlaar, N.J., 2001. Latent heat effects of the major mantle phase transitions on low-angle subduction. Earth Planet. Sci. Lett. 190 (3), 125–135. https://doi.org/10.1016/S0012-821X(01)00383-1. ISSN 0012-821X.

Yang, T., Gurnis, M., Zahirovic, S., 2018. Slab avalanche-induced tectonics in self-consistent dynamic models. Tectonophysics 746, 251–265. https://doi.org/10.1016/j.tecto.2016.12.007.

Zhao, D., Fujisawa, M., Toyokuni, G., 2017. Tomography of the subducting Pacific slab and the 2015 Bonin deepest earthquake (Mw 7.9). Sci. Rep. 7 (February), 1–8. https://doi.org/10.1038/srep44487. ISSN 20452322.